Cement and Concrete Research 160 (2022) 106922

Contents lists available at ScienceDirect

Cement and Concrete Research

journal homepage: www.elsevier.com/locate/cemconres

Dissolution-precipitation reactions of silicate mineral fibers at alkaline pH

Rajeswari Ramaswamy, Juho Yliniemi *, Mirja Illikainen

Fibre and Particle Engineering Research Unit, University of Oulu, P.O. Box 4300, 90014 Oulu, Finland

ARTICLE INFO

Keywords:
Mineral wool
Basalt
Soda-lime glass
Dissolution
Surface precipitates
TEM-EDS
Thermodynamic modelling

ABSTRACT

Silicate mineral fibers – stone (Sw) and glass wool (Gw) – are promising resources for cementitious binders. Insights gained from their dissolution kinetics under alkaline conditions can help to control the release of elements, formation of cementitious phases, and understand reactivity of similar type glasses (soda-lime and basalt). Decreasing the liquid-to-solid ratio (L/S) affects the dissolution rate of Sw, whereas the effect was lower for Gw. Residual rate observed for Sw was due to approaching equilibrium between the surface precipitates and solution chemistry. Two types of precipitation products were observed for both fibers at high pH: Mg-Al-Fe LDH and a C-N-(A-)S-H phase with a small concentration of Al. Dissolved Al was observed to incorporate more in LDH at a high L/S, whereas at a low L/S, Al incorporates more into C-N-(A-)S-H gel, altering its morphology. In addition, Ca-Ti-Si-rich globular domes, and Ca-Fe-Ti-rich nano-dome like hydrogarnets on the Sw fiber surfaces were observed.

1. Introduction

A shortage of landfilling areas and the unrecyclable property of mineral wool wastes have attracted alternative ways to reuse and convert these wastes into secondary raw material [1]. Recently, it has been found that mineral wools can be used as raw material for alkali-activated materials [2,3] or as supplementary cementitious material (SCM) with Portland cement [4,5]. Alkali activation is a process in which reactive aluminosilicate material in the presence of an alkaline activator can form cementitious binders with comparative strength to traditional cement (OPC). Dissolution is the primary step in the alkali activation and cement hydration processes. It involves the breakage of bonds and the release of ionic species from the surface of the material upon interaction with the reacting solution. Dissolved species play a key role in the strength development and structural morphology of the final cementitious binder [6–9]. So far, dissolution studies of mineral wools have been only carried out in acidic and near-neutral conditions to reflect their ability to dissolve in lungs [10–12] and one on dissolution of stone wool at alkaline condition [13]. The main objective of the current study was to investigate and understand the dissolution kinetics and type of precipitation products of both type of mineral wools (Sw & Gw) at (a) both low and high alkaline pH, depicting the pH of Na_2CO_3 and NaOH solutions, and (b) liquid-to-solid ratio (L/S) conditions, depicting far (L/S 1000) and near equilibrium (L/S 50). A better understanding of the dissolution kinetics of mineral wools under alkaline conditions is needed in order to control the release of elements and the precipitation of reaction products, such as N-A-S-H and C-A-S-H hydrates [2,14,15]. Moreover, the findings will help to predict and understand the durability of other silicate materials, such as basalt and soda-lime glass, in alkaline conditions as their composition is similar to that of mineral wools. In Section 2, a brief review of mineral wool composition, structure, and glass dissolution is presented, which will be used as a background to discuss the results in later sections.

2. Background

2.1. Chemical composition and structure of mineral wool

Mineral wools (MW) or silicate mineral fibers (SMF) are amorphous materials that are classified based on the raw material or manufacturing process (fiberization). Stone wool (Sw), often also called rock wool, is a Ca-Mg-Al-Si glass made from basaltic rocks and thus represents a chemical composition similar to that of basalt glass. Glass wool (Gw) composition is similar to that of soda-lime-silicate glass and is manufactured using sand, limestone, soda, and borax, although increasingly higher amounts of recycled waste glasses are currently used as raw material [16,17]. Based on their chemical composition, these mineral wools can be distinguished by the $R_2O/R'O$ ratio in their structure, where R_2O and R'O are the oxides of alkali and alkali earth elements, respectively. For Gw, the ratio is >1; whereas, for Sw, it is ≤1 [18].

* Corresponding author.
E-mail address: juho.yliniemi@oulu.fi (J. Yliniemi).

https://doi.org/10.1016/j.cemconres.2022.106922
Received 16 September 2021; Received in revised form 12 July 2022; Accepted 16 July 2022
Available online 27 July 2022

Silicate glasses in general are disordered metastable structures composed of polymeric networks in which oxygen ions are covalently bonded to Si ions in a tetrahedral geometry (Fig. 1a). These glasses are composed of network formers with coordination number 4 (acidic oxides SiO_2, B_2O_3, P_2O_5, ZrO_2) and network modifiers (basic oxides CaO, MgO, FeO, Na_2O, K_2O) with coordination number ≤ 6. Al_2O_3 and TiO_2 are amphoteric oxides that can act as both a former and a modifier and are called intermediates or stabilizers—but, in most cases, they are considered network formers. The oxygen that is bonded to two network-forming cations is called bridging oxygen (BO). The oxygen that gets bonded to the network-modifying cation is called non-bridging oxygen (NBO). Since the forces between the oxygen and the modifier cation are smaller, the bond can be easily broken down compared to the strong Si-O-Si bonds. The greater the NBO/BO ratio in the glass structure, the easier it is to break the network due to the increased degree of depolymerization [17-20].

2.2. Dissolution of silicate glasses

The dissolution of glass is a complex process that can be (i) congruent (surface-controlled/stoichiometric release of ions), (ii) incongruent (diffusion-controlled/leaching/selective/non-stoichiometric release), or (iii) dissolution, involving selective dissolution and congruency [21]. Dissolution kinetics depend mainly on the glass composition [22,23], reacting liquid chemistry (pH) [14,24,25], presence of aqueous elements such as Ca [14,26,27], Mg [28], Fe [29], and Al and Si [30], temperature [14,22,31], L/S, and the surface area of glass to solution volume (SA/V or S/V) [23,32]. At high pH, (pH >9), dissolution occurs predominantly by silicate network hydrolysis and dissociation of the silicate network into $Si(OH)_4$, $H_3SiO_4^-$, and $H_2SiO_4^{2-}$ species [33].

At Stage I, a combination of ion-exchange reactions with protons occurs, which increases the pH and initiates the hydrolysis of the silicate network (Fig. 1b). The initial dissolution rate is the maximum forward rate at which there is no response of the dissolved species back to the glass. After prolonged dissolution, the dissolved silicate and aluminate species react with other metal ions in the solution and may reach saturation of certain solid phases. The rate drop (Stage II) with a residual rate regime (quasi-steady state-Stage III) may be observed for several reasons: (1) due to the chemical affinity between glass and/or precipitate and solution (thermodynamic equilibrium), (2) due to silicon saturation in the solution, which reduces the affinity for hydrolysis [22,34], or (3) due to the dense protective gel layer, which can be passivating and transport-limiting for aqueous species (kinetic property) [31,35–37]. The resumption (Stage IV) of the dissolution rate at later stages occurs by the precipitation of crystalline phase-like zeolites [38], which either changes the chemical affinity or brings the silicon concentration under the saturation limit; or by destabilization of the passivating gel layer properties either by dissolving or consuming the elements from the gel. This stage is observed mainly at alkaline conditions, high temperatures, high SA/V conditions, and with alkali-rich or Al-rich glass compositions [39,40].

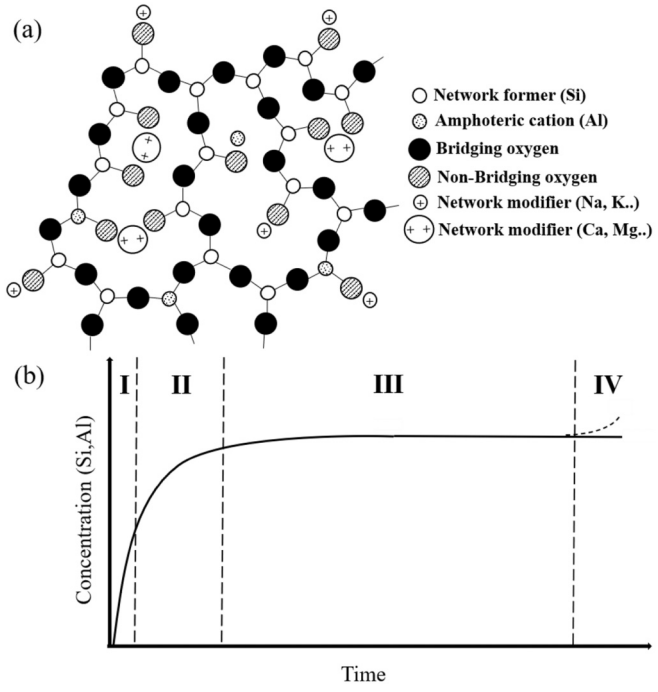

Fig. 1. Schematic representation of (a) silicate glass structure, (b) different rate stages and mechanisms of glass dissolution (concentration of dissolved species versus time). **I**: initial rate (including interdiffusion and hydrolysis); **II**: rate drop; **III**: residual rate; **IV**: resumption of dissolution.

3. Materials and methods

3.1. Sample characterization

Two different types of mineral wools—Sw and Gw without organic resin coating or other additives that are typically applied on them—were used. Mineral wools were crushed using a hydraulic press (20 kN for a cylinder press 5 cm in diameter) and sieved to a particle size $\leq$45 μm. Sieving was done to reduce the number of shots present in Sw [16] and to have a uniform treatment for both materials. Sieved material was stored in a desiccator to avoid any reaction with atmospheric moisture. The composition of the mineral wools (in wt%) was determined by X-ray fluorescence (XRF) from a melt-fused tablet and lighter element (such as boron) composition present in mineral wool (especially in Gw) was determined by inductively coupled plasma optical emission spectrometry (ICP-OES) by acid digestion of the mineral wool powder. The density of the sieved material was determined by helium pycnometry (Micromeritics AccuPyc II 1340), and the specific surface area was determined by the multipoint Brunauer-Emmett-Teller (BET) method using N_2-adsorbent gas. The results are presented in Table 1.

3.2. Dissolution methodology

Experiments were carried out at room temperature (22 °C). All bottles used in the experiments were prewashed with 2 cycles of diluted HNO_3/HCl and deionized water and then dried before use. Dissolution experiments were conducted in a N_2-filled Atmos bag. NaOH solutions were made at concentrations of 1 mM and 1 M using analytical-grade NaOH pellets from Sigma Aldrich and ultra-high-quality Milli-Q water (resistivity 18.3 MΩ). Before commencing the experiment, NaOH solutions were bubbled with N_2 gas to de-aerate and minimize the effect of CO_2 on dissolution. Sieved mineral wool powder was added to NaOH solutions containing 250 ml polypropylene bottles and stirred with a horizontal shaker at 250–300 rpm. After each specific reaction time, bottles were removed from the glove box and the suspension was first filtered using 2–5-μm pore diameter Whatman filter paper and then the filtrate was passed through a 0.45-μm pore filter syringe. The solution was acidified with 2 % HNO_3 solution and stored at 4 °C until ICP-OES analysis. Solids were washed with cold isopropanol to stop further dissolution, then air-dried and stored in a desiccator for further analysis. The reproducibility of the ICP results had a variation of $\leq\pm$10 %. The pH of the solutions was measured before and after dissolution tests, and the pH variation was <0.1 pH units.

The experiments were conducted to study the mineral wool initial dissolution kinetics at both pH 11 and pH 14 with an L/S ratio of 1000 for 7 days. To study the effect of the L/S ratio, 1 M NaOH was used and dissolution experiments were conducted for 30 days at far from equilibrium (L/S 1000) and near equilibrium (L/S 50). Sample codes are used throughout this paper to identify the sample types (S for stone wool

Table 1
Elemental composition (in wt%) of major elements and physical properties of the mineral wools.

Sample	Elemental composition (wt%)											Density (g/cm^3)	BET (m^2/g)
	O	Si	Al	Ca	Mg	Fe	Na	K	Ti	B	Others[a]		
Sw	42.7	18.9	8.4	13.1	7.2	4.7	1.1	0.7	0.9	0.0	0.83	2.9	0.2385 ± 0.006
Gw	46.7	29.6	0.8	5.9	1.9	0.3	10.7	0.4	0.0	1.7	0.54	2.7	0.3388 ± 0.002

[a] For detailed elemental composition, see Supporting Information Table S1.

and G for glass wool) with their respective parameters, L/S ratio (1000 or 50), NaOH molarity (1 mM or 1 M), and time in days (0–30 d) or hours ($0-20h$). The sample code used has the following structure: $\frac{\mathbf{L}}{\mathbf{S}}\mathbf{ratio}_{\mathbf{Time}}$ **Sample type**$_{\mathbf{Molarity}}$. For example, $^{\mathbf{1000}}_{\mathbf{7d}}\boldsymbol{S_{1M}}$ corresponds to **S**w with an L/S ratio of **1000**, a concentration of NaOH **1 M,** and a dissolution period of **7 d**.

The normalized mass loss *NL* (μg/cm^2) of element *i* within the mineral wool gives information on the reaction progress, which was calculated using Eq. (1) [31]. The extent of the dissolution (E_i) of the mineral wool (%) of element *i* for a given molarity and L/S ratio was calculated by Eq. (2). However, precipitation reactions will affect the real value of the elemental mass loss and eventually the extent-%, but it can be used to understand and track different regimes of the dissolution-precipitation process of the mineral wool with respect to time.

$$NL_i = \frac{C_i{*}V{*}10^6}{SSA{*}m{*}X_i} \quad (1)$$

$$E_i\ (\%) = \frac{C_i{*}V}{m{*}X_i}{*}100 \quad (2)$$

where C_i is the concentration of the element released (g/L) (based on ICP results), *V* is the volume of the NaOH solution (L), *m* is the mass of the mineral wool (g), *SSA* is the initial specific surface area of mineral wool powder (cm^2/g) (based on the BET analysis), and X_i is the mass fraction of element *i* from the mineral wool composition (based on the XRF analysis).

To understand and compare the reaction kinetics of both mineral wool at different pH, the normalized initial dissolution rate Nr_i (μg/cm^2/h) (until 10 h in this study) was calculated using Eq. (3) only for a very dilute experimental condition (such as L/S 1000) where precipitation of Si is minimized. However, the rate drop values were not calculated due to precipitation reactions which can underestimate the real value and residual rate was calculated to only to those where the regime is observed to occur.

$$Nr_i = \frac{dNL_{Si}}{dt} \quad (3)$$

Theoretical and experimental elemental concentration data were used to perform geochemical modelling with the PHREEQC software using the CEMDATA (version 18.1) database [41]. This modelling was performed to thermodynamically determine the saturation indices of potential solid phases. The theoretical elemental concentrations of all other elements (in mg/L) in the mineral composition were calculated with respect to the extent of dissolution of Si (E_{Si}), assuming that the congruent dissolution of the mineral wool occurred at high pH conditions using Eq. (4):

$$\text{Theoretical elemental concentration of i} = \frac{E_{Si}{*}m{*}X_i}{100{*}V} \quad (4)$$

3.3. Characterization of solid products after dissolution

High-resolution images of the precipitation products and the morphology of the fibers were analyzed with a Zeiss sigma field emission scanning electron microscope (FE-SEM) equipped with energy-dispersive x-ray spectroscopy (EDS) for elemental analysis. The acceleration voltages of 5 kV and 15 kV were used for imaging and EDS analysis, respectively. Dried solids were spread on a carbon tape and coated with platinum or carbon depending on the analysis. A JEOL JEM-2200FS scanning transmission electron microscope (STEM) equipped with EDS with an acceleration voltage of 200 kV and working depth of 1–2 μm was used for characterization of the elemental composition of the surfaces of the fibers by square (area under square drawn on the precipitates) and area (area under free form-scribbles drawn on the precipitates) analysis of elemental mapping. Powder X-ray diffraction (XRD) was performed using Rigaku SmartLab with a Cu source lamp of 40 kV and 135 mA. The crystalline phases were identified using PDXL2 software with the ICDD PDF4+ 2015 database.

4. Results

4.1. Solution chemistry (ICP-OES)

The results show that in the 1 mM NaOH solution, the elements were released in a similar pattern for both Sw and Gw (Fig. 2). In $^{\mathbf{1000}}\boldsymbol{S_{1mM}}$ in Fig. 2a, NL_{Ca} and NL_{Mg} was higher compared to NL_{Si} and NL_{Al} showing that Ca and Mg leached out in the initial stages (between 1 h to 10 h) of the experiment with respect to Si. Mg reached its maximum normalized mass loss (NL_{Mg}) at 10 h, after which it remained constant, indicating possible precipitation of the Mg phases (shown in later sections). Ca showed congruent normalized mass loss in respect to Si between 10 h and 1 d, after which the mass loss of Ca was greater than that of Si. This may be due to either leaching of Ca ions from the mineral wool surface or precipitation of the Si phases. Al mass loss was congruent with respect to Si for the first 10 h but started to decline exactly after 10 h, indicating possible formation of Al precipitates.

Similarly, as in the case for Sw, modifier ions Ca and Mg in Gw ($^{\mathbf{1000}}\boldsymbol{G_{1mM}}$) leached out for 10 h, after which the dissolution was nearly stoichiometric in relation to Si until 3 d (Fig. 2b). Between 3 to 7 d, NL_{Ca} was slightly lower compared to NL_{Si}, indicating precipitation of Ca. NL_{Mg} was low particularly after 3 d, but the concentration was increasing even after 7 d. NL_{Al} was congruent with respect to NL_{Si} for the first 24 h, after which the Al mass loss was lower than that of Si but equal to NL_{Mg}. NL_{Fe} was not shown as Fe was under the detection limit of the ICP method used throughout the 7-d experiments for both mineral wools, indicating precipitation with very low concentrations (concentrations <0.016 mg/L).

Fig. 3 shows the NL_i versus time for Sw in 1 M NaOH with two different L/S ratios. At initial stages, Ca and Al were preferably released over Si at L/S 1000, whereas a stoichiometric release was observed with L/S 50. In sample $^{\mathbf{1000}}\boldsymbol{S_{1M}}$, Ca and Al leached out until 1 d, after which the dissolution was nearly congruent with respect to Si until 5 d. NL_{Ca} started to decrease after 5 d to 30 d, indicating Ca precipitation. NL_{Al} continued to increase more with respect to NL_{Si} from 5 d to 30 d. In $^{\mathbf{50}}\boldsymbol{S_{1M}}$, Al was stoichiometrically released with Si until 1 d, and NL_{Ca} was nearly congruent for the first 10 h of the experiment. NL_{Ca} started to decrease after 10 h to 30 d, whereas NL_{Al} continued to increase between 1 d and 30 d with respect to NL_{Si}. A clear effect by the L/S ratio was observed on the NL_i values at all stages of dissolution. For $^{\mathbf{1000}}\boldsymbol{S_{1M}}$, Si and Al reached saturation with the solution between 15 d and 25 d, but there was a slight increase in their mass loss at 30 d. For $^{\mathbf{50}}\boldsymbol{S_{1M}}$, Si and Al

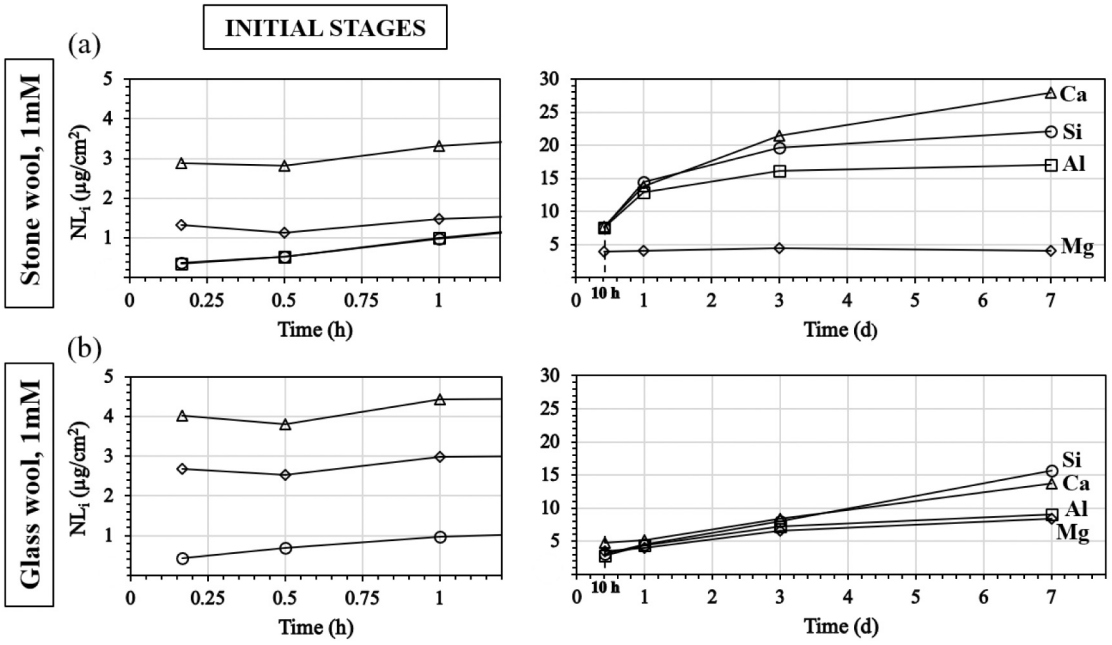

Fig. 2. Normalized mass loss (NL_i) versus time for (a) Sw and (b) Gw in 1 mM NaOH. The left-hand side of the figure represents the initial stages (0−1 h), and the right-hand side represents NL_i between 10 h and 7 d [Under the detection limit: Fe for both mineral wools until 7 d, Al for Gw during the initial stages]. Reproducibility of the ICP results had a variation of ≤±10 %.

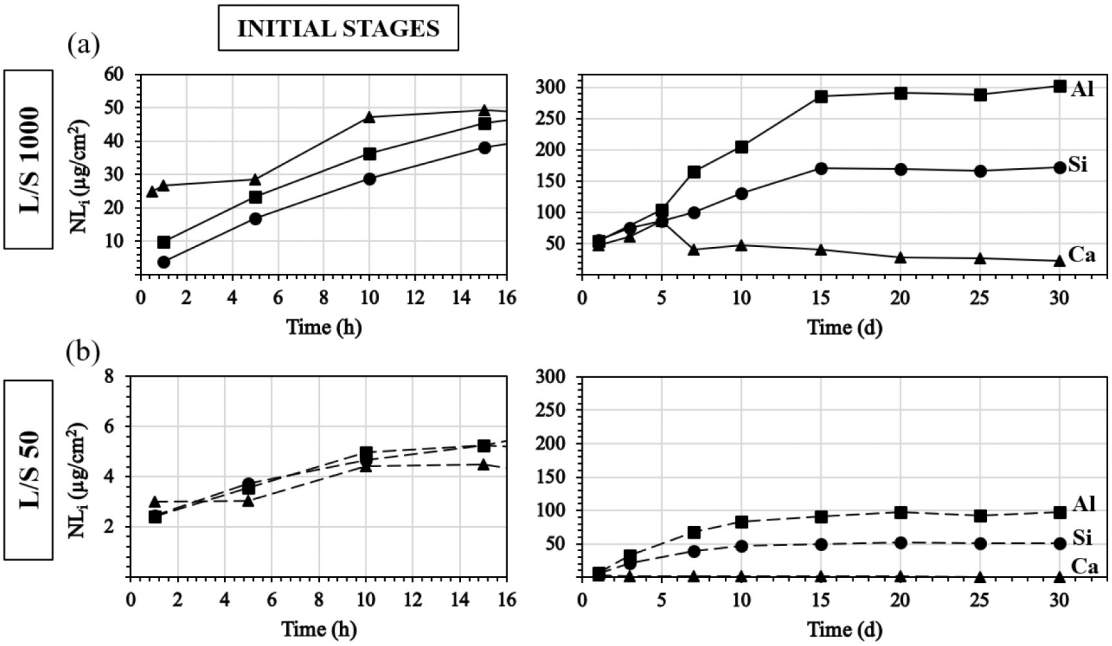

Fig. 3. Normalized mass loss versus time for dissolution of Sw in 1 M NaOH at (a) L/S 1000 and (b) L/S 50. The left-side graphs represent the initial stages (0–15 h), while the right-side graphs represent NL_i from 1 d to 30 d [Under the detection limit: Fe and Mg until 30 d]. Reproducibility of the ICP results had a variation of ≤±10 %.

reached saturation with the solution between 10 d and 30 d. NL_{Si} values at both L/S were lower than NL_{Al} values at later stages, indicating possible precipitation of the Si phases. The NL of Mg and Fe was not included as their elemental release was under the detection limit of the ICP-OES (2.1 mg/L and 1.3 mg/L, respectively) at both L/S ratios, indicating their precipitation.

Fig. 4 shows the NL_i versus time for Gw in 1 M NaOH at two different L/S ratios. The NL_i during the initial stages was affected by the L/S ratio, whereas the NL_i was not affected at the later stages (including precipitation reactions). Unlike in the case of Sw, a linear mass loss of Si was observed at both L/S ratios for Gw within the experimental period. However, at initial stages, Al and Ca were leached out over Si at L/S 1000, like in the case of Sw, whereas a nearly stoichiometric release was observed with L/S 50. In sample $^{1000}G_{1M}$, Al and Ca leached out until 1 d and 15 d, respectively. NL_{Ca} started to decrease from 15 d, whereas NL_{Al} was nearly congruent or lower compared to NL_{Si} until 30 d. In $^{50}G_{1M}$, the NL of Al and Ca was nearly congruent with respect to Si for the first 10 h. A varying decrease and increase were observed for NL_{Ca}

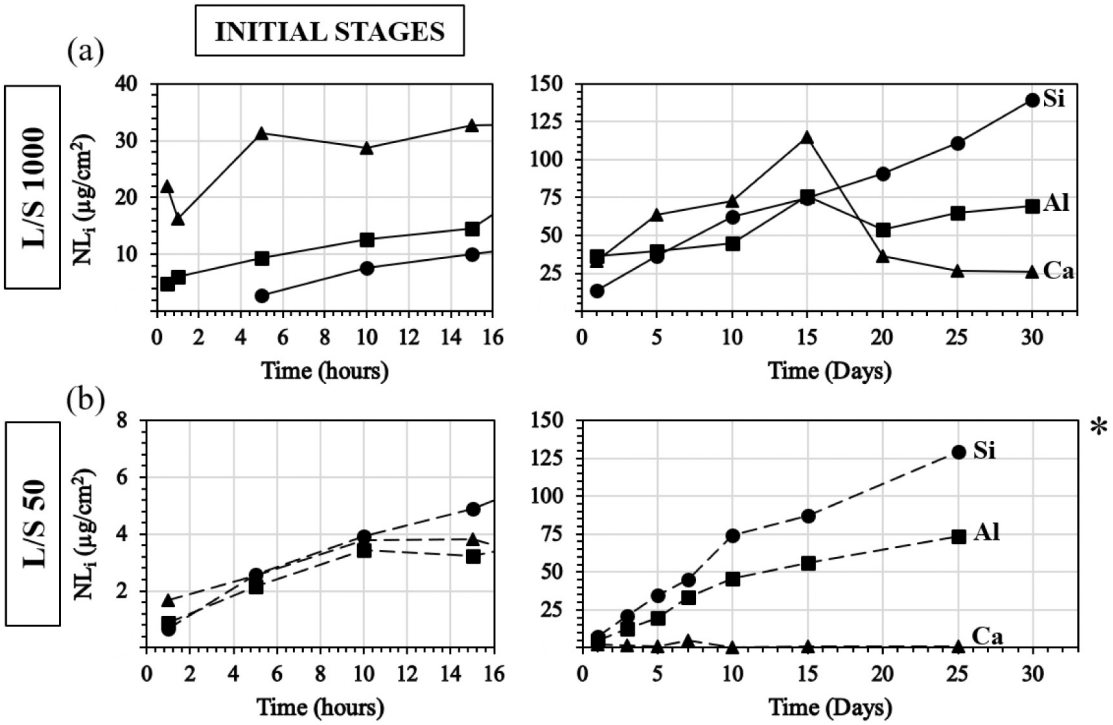

Fig. 4. Normalized mass loss versus time for dissolution of Gw in 1 M NaOH at (a) L/S 1000 and (b) L/S 50. The left-side graphs represent initial stages (0–15 h), while the right-side graphs represent NL_i from 1 d to 30 d. * $^{50}_{30d}\mathbf{G_{1M}}$ NL_i data was not included due to stable gel formation occurring in the sample before carrying out ICP analysis [Under the detection limit: Fe and Mg until 30 d, Si for L/S 1000 initial stages until 5 h]. Reproducibility of the ICP results had a variation of $\leq \pm 10$ %.

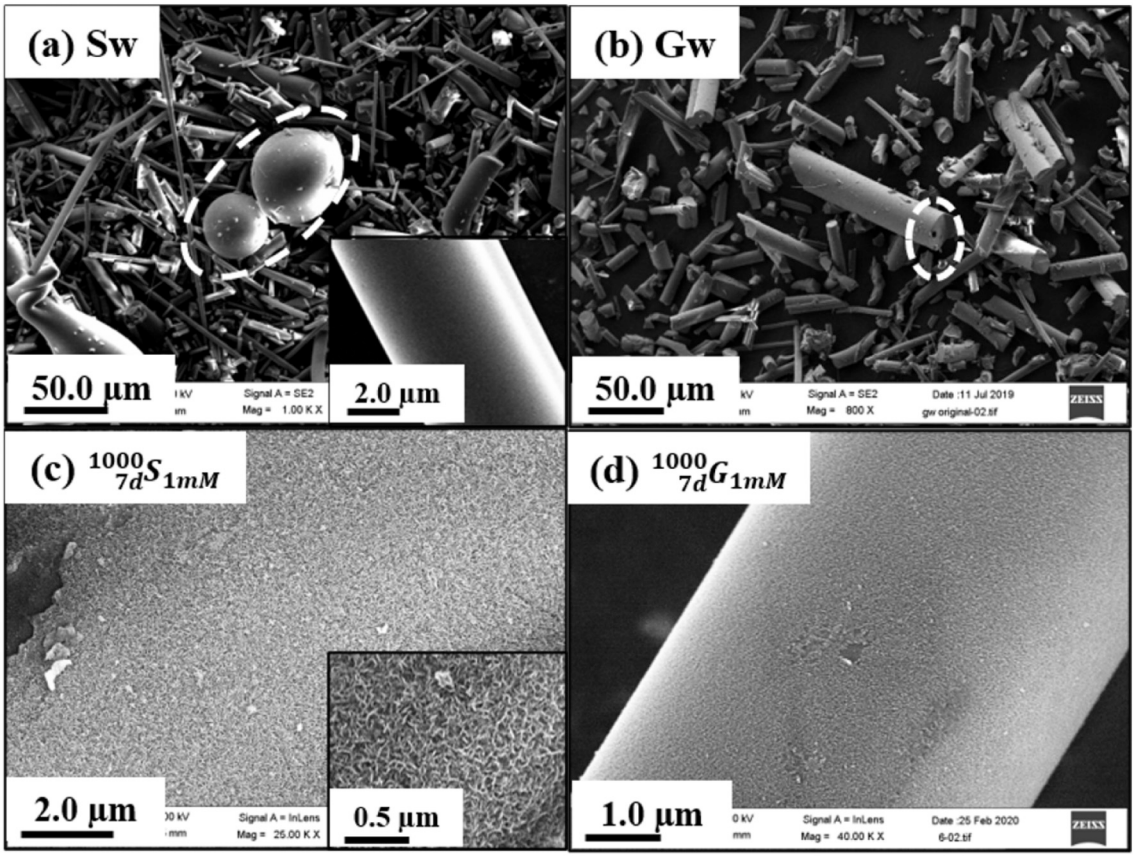

Fig. 5. SEM images of (a) unreacted Sw [the dashed white circle shows "shots" and a magnified image of the fiber surface], (b) unreacted Gw [the dashed white circle shows the hollow in the center of unreacted fibers] and surface precipitates of dissolution samples after 7 d in 1 mM NaOH at L/S 1000, (c) nano-porous platelet-like precipitate on Sw, and (d) thin layer-like precipitate covering the entire Gw fiber surface.

from 15 to 25 d, indicating changes in precipitation reactions. NL_{Al} was lower compared to NL_{Si} between 3 d and 25 d, indicating precipitation of Al. Like in the case of Sw, the NL of Mg and Fe was not included in Fig. 4 as they were under the detection limit of the ICP-OES at both L/S ratios, indicating precipitation.

4.2. Morphology & elemental composition of surface precipitates (SEM-EDS)

The surface morphology of the fibers before and after each dissolution period was studied by SEM. The unreacted fibers of both mineral wools had a smooth surface, as shown in Fig. 5a and b. The fibers had different diameters, and some fibers had a partly hollow center (as marked in a white dashed circle, shown in Fig. 5b), which were observed in both mineral wools. In Sw, due to its production method, "shots" (spherical in shape, ≤60 μm) were produced along with the cylindrical fibers (as marked in a white dashed circle, shown in Fig. 5a) [16]. After sieving, most of the shots are removed, as discussed in the experimental Section 3.1, so they were not present in the dissolution experiments. After the dissolution test, both fiber types were covered with surface precipitates independent of the L/S ratio and NaOH molarity (Figs. 5c-d, 6, and 7). For $^{1000}S_{1mM}$, a thin precipitate layer covered the Sw fibers, which was already visible after 0.5 h of dissolution (see Supporting Information, Fig. S1a), and from 10 h onwards (Fig. S1b), a nano-porous,

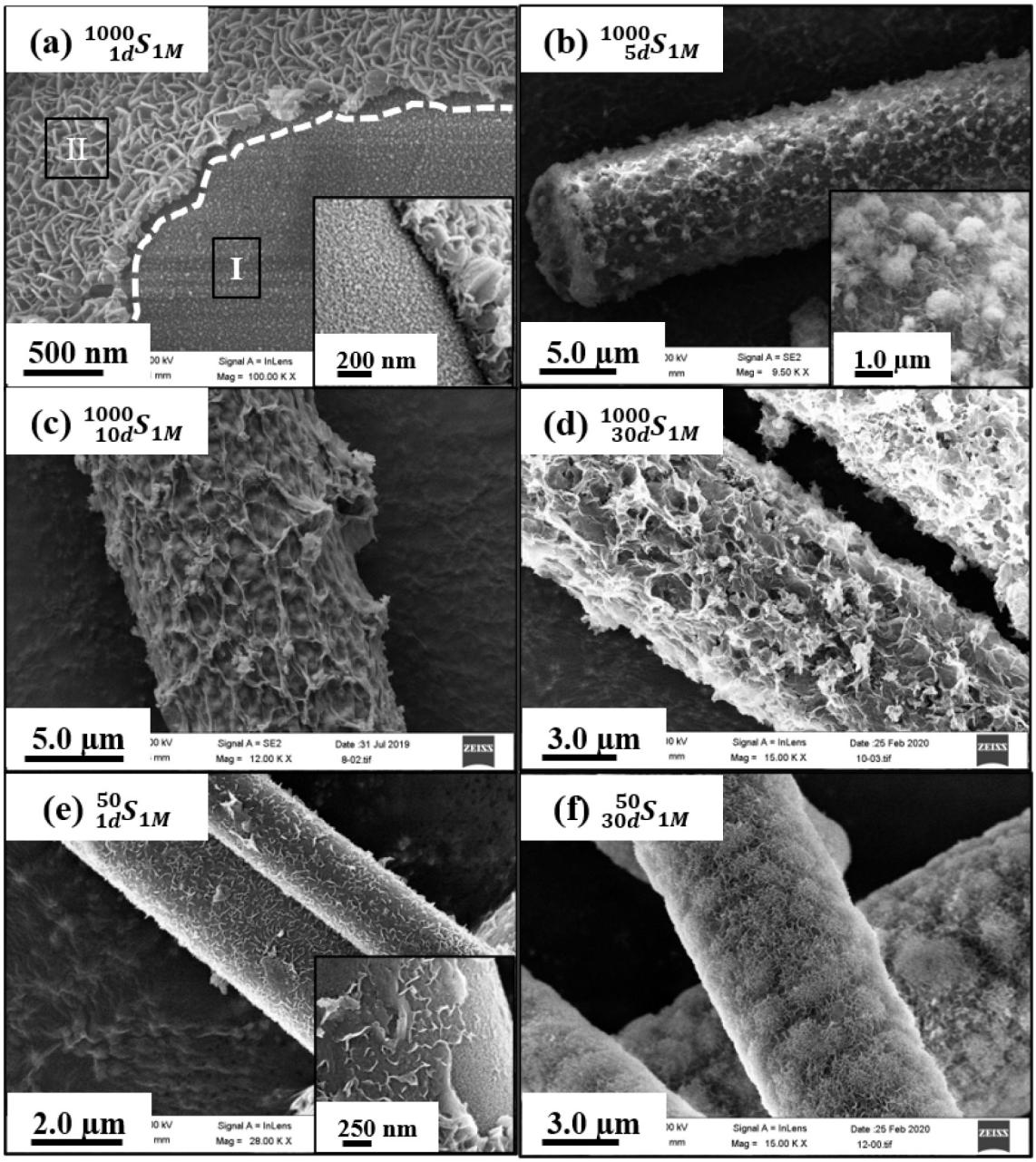

Fig. 6. SEM images of Sw fiber surface after respective dissolution period in 1 M NaOH (a) after 1 d at L/S 1000 – area I and magnified image shows the numerous nano-spherical dome structures present under the nano-porous, platelet-like precipitates (area II) covering the entire fiber, (b) after 5 d at L/S 1000 – globular micro dome structures (also shown in the enclosed magnified image) on top of the nano-porous, platelet-like precipitates, (c) after 10 d at L/S 1000 – shows the film-like layer covering the entire fiber surface, (d) after 30 d at L/S 1000 – shows the flaky/fibrous porous precipitate, (e) after 1 d at L/S 50 – shows non-porous platelets with *meso* circular pillar like precipitates (shown in enclosed magnified image), and (f) after 30 d at L/S 50 – shows the flaky/fibrous porous precipitate covering the fiber surfaces.

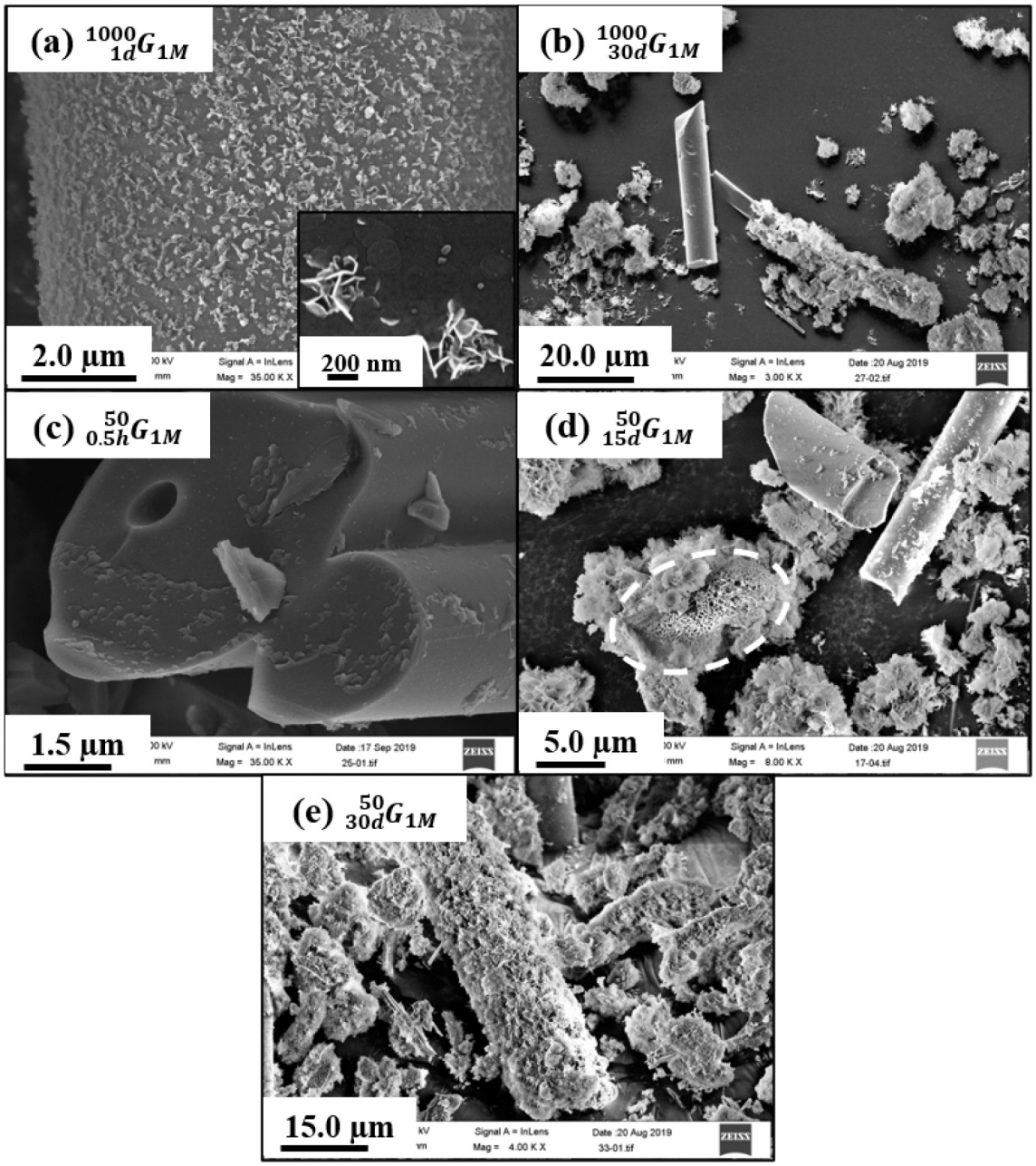

Fig. 7. SEM images of Gw fiber surface after respective dissolution period in 1 M NaOH at different times: (a) after 1 d at L/S 1000, showing a non-porous platelet like precipitate that did not cover the entire surface, (b) after 30 d at L/S 1000, showing a flaky/fibrous porous precipitate on fibers that were easily detached from the fiber surfaces during SEM preparation, (c) after 0.5 h at L/S 50, showing a thin precipitate layer covering the fiber surfaces, (d) after 15 d at L/S 50, showing a flaky porous precipitate [dashed white circle area showing the presence of a nano-porous, platelet-like precipitate layer under the flaky porous precipitate detached from the fiber surface], and (e) after 30 d at L/S 50, showing the flaky porous precipitate covering the fiber surfaces.

platelet-like precipitate started to form until 7 d (Fig. 5c). For $^{1000}G_{1mM}$, the formation of a thin layer- like precipitate around the fiber was observed at 7 d (Fig. 5d) before that the surface had a smooth texture same as the original fiber until 3 d.

The formation of surface precipitates during the experiments was particularly diverse in the case of $^{1000}S_{1M}$ (Fig. 6a–d). First, from beginning of 10 min of the dissolution, a nano-porous, platelet-like precipitate started to form until 3 d, covering the entire fiber (area II, as shown in Fig. 6a). Underneath this layer, the fiber surface was covered with nano-spherical domes, which was revealed by stripping off the fiber covered with platelet precipitates during the SEM sample preparation (area I and magnified SEM picture of area I in Fig. 6a). After 5 d of the experiment, globular micro dome structures were observed on top of the platelet layer (see magnified SEM picture in Fig. 6b). Around 10 d, the fibers were entirely covered with a film-like layer (Fig. 6c) and, around 15 d, on top of this film-like layer, a flaky/fibrous porous structure formation was observed until 30 d (Fig. 6d).

The L/S ratio influenced the time of the precipitate formation and the surface morphology of the precipitation products. Unlike in the case of $^{1000}S_{1M}$, only two main types of precipitates were observed in the case of $^{50}S_{1M}$ (Fig. 6e and f). For sample $^{50}S_{1M}$, after 0.5 h of the experiment, the fibers were covered with a thin layer-like precipitate (Fig. S1c) and, from 10 h, a platelet-like precipitate (Fig. 6e) started to form—but they were not porous, as was the case for sample $^{1000}S_{1M}$ after 1 d. The magnified image in Fig. 6e shows meso circular-like pillar structures formed along with the platelets. Starting from 2 d, the flaky/fibrous porous structure

started to form until 30 d (Fig. 6f). The flaky/fibrous precipitation products had differences in porosity and adhesion to the fibers, i.e., for $^{1000}_{30d}S_{1M}$, the precipitate had large pores and was weakly attached to the fiber; whereas for $^{50}_{30d}S_{1M}$, the precipitate had a network of very small pores and was strongly attached to the fiber. This strong or weak attachment of the precipitate to the fibers was concluded from their resistance to SEM sample preparation. The globular micro dome structure formed on top of the nano-porous, platelet-like structure in $^{1000}S_{1M}$ was not observed in the case of $^{50}S_{1M}$.

For $^{1000}G_{1M}$, the SEM images show the formation of nano-porous, platelet-like precipitates at 1 d, which did not cover the surface fully (Fig. 7a), as was observed for $^{1000}S_{1M}$ (Fig. 6a area II) which can be due to low availability of Al and Fe in the composition of Gw. This layer was followed by the formation of a flaky/fibrous porous structure from 15 d until 30 d (Fig. 7b). With a lower L/S ratio ($^{50}G_{1M}$), the surface of the Gw fibers was covered with a thin layer-like precipitate already after 0.5 h (Fig. 7c), but the presence of nano-porous platelets was not observed at 1 d, as was seen in $^{1000}G_{1M}$. The flaky/fibrous porous precipitate started to form from 3 d to 30 d (Fig. 7e). From Fig. 7d, the area marked with a white dashed circle indicates that the detached precipitation product had a nano-porous, platelet-like precipitate layer underneath the flaky/fibrous porous structure, indicating the formation of the precipitate with time.

The surface precipitates were analyzed with EDS analysis (both point analysis and elemental mapping). Due to the limits of the EDS technique, the precipitates could be analyzed only after they reached a certain thickness ($\geq$ 1 μm) [42], and thus the results are shown only for the samples of later stages of the experiments. Nevertheless, the $^{1000}_{1d}S_{1M}$ sample fiber surface was analyzed by EDS to gain elemental information on the nano-spherical domes (area I) present below the nano-porous, platelet-like precipitate. The point analysis showed that the fiber was enriched with Ca, Fe and Ti (see Supporting Information, Table S2 and Fig. S2). Elemental mapping of the $^{1000}_{10\ d}S_{1M}$ sample, where the fiber was covered with the film-like layer (Fig. 6c), was found to be rich in Ca (see Supporting Information, Fig. S3). EDS analysis (point analysis in Table 2 and elemental mapping shown in Supporting Information Fig. S4 a & b) of fibers after dissolution times at later stages (Fig. 8a and b) showed that Sw was covered with two distinctive precipitation products—one rich in Mg, Fe, and Ti (nano-porous, platelet-like precipitate) and the other rich in Na, Ca, and Si (C-N-(A-)S-H type gel, flaky/fibrous porous-like precipitate). From Fig. 8a, it can be observed that the fiber was surrounded with a concentric circular layer of the Mg- and Fe-rich layer and then the flaky/fibrous porous C-N-(A-)S-H rich layer after 15 d (Table 2). This indicates that the Mg-Fe-rich layer continued to precipitate and form around the dissolving fiber, where the C-N-(A-)S-H layer grew around the Mg-Fe-rich layer. EDS analysis (Table 2) of the Gw in the case of the $^{50}_{30d}G_{1M}$ sample (Fig. 8c) showed that the flaky porous precipitation product contains in Na, Ca, Mg and Si. The elemental composition of the precipitates was investigated in more detail by the TEM technique, and the results are presented in the next section.

4.3. Elemental composition of surface precipitates (STEM-EDS)

STEM coupled with EDS was used to provide semi-quantitative elemental information of the precipitation products formed on the fiber after the respective dissolution times. TEM results strongly correlate with the elemental information attained from the SEM results. Samples $^{1000}_{1d}S_{1M}$ (Fig. 9a), $^{1000}_{1d}S_{1mM}$ (Fig. 9b), and $^{1000}_{7d}S_{1mM}$ (Fig. 9c) had a nano-porous platelet morphology but differed in the amount of elements present in them, as shown in Table 3. EDS results showed that the surface precipitates on $^{1000}_{1d}S_{1M}$ were mostly rich in Mg, Fe, and Ti; whereas for $^{1000}_{1d}S_{1mM}$ and $^{1000}_{7d}S_{1mM}$, they were rich in Mg, Fe, Al, and Si. Some precipitates were thin and were observed to decompose due to the high accelerating voltage, for example, hydrotalcite like precipitates (Fig. 9a) and the phyllosilicates (Fig. 9b) on SW [21]. In this case the intensity of the electron beam was reduced by introducing smaller aperture and increasing scanning speed. In this way, reliable EDS data was obtained (Table 3). The flaky/fibrous porous precipitate of $^{1000}_{30d}S_{1M}$ (Fig. 9d) was rich in oxides of Na, Ca, and Si, and the globular dome structures that are clearly visible in the elemental mapping were rich in Ca, Ti and Si.

Samples $^{1000}_{30d}S_{1M}$ and $^{50}_{30d}S_{1M}$ differed only by the L/S ratio, but a difference in the precipitates was observed. For L/S 50 (Fig. 9e), the Al, Si, and Ti incorporation in the flaky porous precipitation product was increased. This increase in concentration may be the reason for the formation of a high, small porous network of the precipitation product. From Table 3, it is evident that the fiber core of $^{1000}_{30d}S_{1M}$ and $^{50}_{30d}S_{1M}$ was rich in Mg, Fe, Al, and Ti, while Mg and Fe were not detected in the flaky porous precipitate, which correlates with the EDS results in Section 4.2. This confirms that the Mg- and Fe-rich precipitates formed toward the dissolving fiber core, while the C-N-(A-)S-H precipitates formed on top of the Mg—Fe precipitate layer, as shown in the SEM-EDS section of Table 2. For $^{1000}_{30d}G_{1M}$ and $^{50}_{30d}G_{1M}$ (Fig. 9f and g), the flaky/fibrous porous precipitates were easily detached from the fiber during TEM sample preparation. This shows that these precipitates were weakly attached to the fiber. These detached precipitation products were observed to be a mix of two phases: an Mg-Fe-rich phase and an C-N-(A-)S-H rich phase, which was the same for Sw.

4.4. Identification of crystalline phases (XRD)

XRD identified and gave information about the crystalline phases formed after the respective dissolution times of the mineral wool. XRD had a detection limit of $\geq$5 wt% for the crystalline phases [42], and thus the precipitates detected by SEM and STEM were not necessarily detectable by XRD. Both mineral wools before dissolution had an amorphous hump but no crystalline peaks. For $^{1000}_{30d}S_{1M}$, $^{50}_{30d}S_{1M}$, $^{1000}_{30d}G_{1M}$, and $^{50}_{30d}G_{1M}$ (Fig. 10), the main crystalline phases formed regardless of the L/S ratio were hydrotalcite $Mg_{0.64}\ Al_{0.36}\ (CO_3)_{0.18}\ (OH)_2\ (H_2O)_{0.46}$) (PDF 04-015-1684), poorly crystalline calcium silicate hydrate $Ca_{1.5}SiO_{3.5}$. xH2O (C-S-H) (PDF 00-033-0306), and calcite

Table 2
EDS averaged elemental composition (in at.%) of the raw material and precipitation products after respective times for both mineral wools. (Note: point analysis was carried out on uneven areas of the precipitate so the values are semi-quantitative).

Elements	Sw					Gw	
(at. %)	Raw material	Dissolution				Raw material	Dissolution
		15 d		30 d			30 d
		a	b	c	d		e
Si	16	3.4	4.9	2.5	4.7	22	7.4
Al	7.4	2.1	0.74	1.7	0.67	0.58	0.41
Ca	8.6	2.6	4.4	2.2	4.5	2.9	2.8
Mg	6.6	7.9	2.2	7.4	2.1	1.6	1.4
Na	0.97	1.3	1.9	2.3	2.7	9.7	4.4
Fe	2.0	1.7	0.52	1.8	0.46		–
Ti	0.49	0.29	0.16	0.29	0.13		–

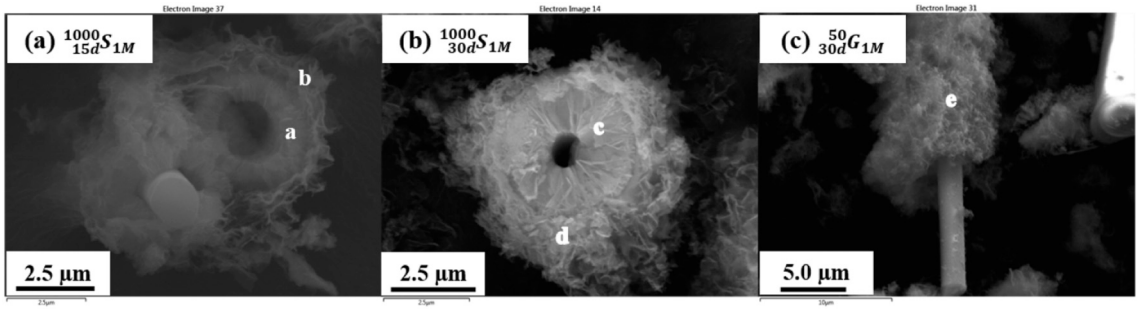

Fig. 8. SEM-EDS images of precipitation products in 1 M NaOH of (a) Sw after 15 d at L/S 1000, (b) Sw after 30 d at L/S 1000, and (c) Gw after 30 d at L/S 50.

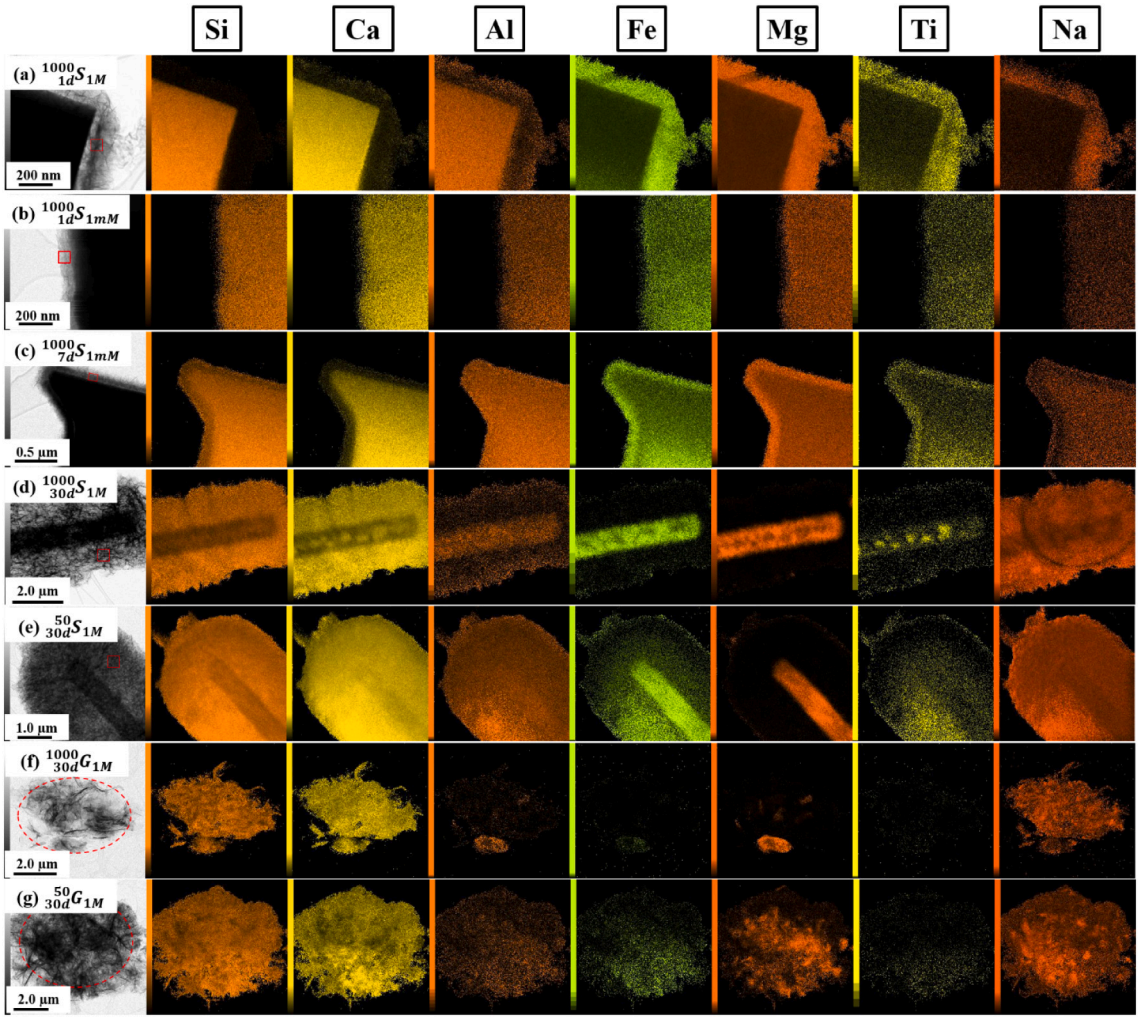

Fig. 9. TEM images of precipitation products of samples (a) $^{1000}_{1d}\mathbf{S_{1M}}$, (b) $^{1000}_{1d}\mathbf{S_{1mM}}$, (c) $^{1000}_{7d}\mathbf{S_{1mM}}$, (d) $^{1000}_{30d}\mathbf{S_{1M}}$, (e) $^{50}_{30d}\mathbf{S_{1M}}$, (f) $^{1000}_{30d}\mathbf{G_{1M}}$, and (g) $^{50}_{30d}\mathbf{G_{1M}}$. Red square in b) and dashed red circle in f) are areas analyzed with mapping tool (values are presented in Table 3). (For interpretation of the references to colour in this figure legend, the reader is referred to the web version of this article.)

$CaCO_3$ (PDF 04-020-5889). XRD showed peaks corresponding to the C-S-H phase for all 1 M samples of both mineral wools, but SEM- and STEM-EDS-analysis also showed the presence of sodium in their structure. Some signals for crystalline structures were observed in the XRD spectra of $^{1000}_{7d}\boldsymbol{S_{1M}}$, $^{50}_{7d}\boldsymbol{S_{1M}}$, and $^{50}_{7d}\boldsymbol{G_{1M}}$ similar to their respective 30 d samples, whereas no crystalline structures were observed in any of the 1 mM samples or in $^{1000}_{7d}\boldsymbol{G_{1M}}$ (see Supporting Information, Fig. S5). This shows that the nano-porous, platelet-like precipitates in $^{1000}_{7d}\boldsymbol{S_{1mM}}$ may be an amorphous analogue of smectite clay rich in Mg, Fe, Si, and Al (phyllosilicates) due to their limited abundance and crystallinity degree, as crystallinity increases with time [43]. The XRD and STEM/EDS results correlate with each other well. Both Sw and Gw have a similar type of major precipitation phases, indicating that the formation of precipitation products is dependent on the saturation limit of the respective phases but the amount of precipitation products might vary.

4.5. Thermodynamic modelling

Thermodynamic calculations provide information on the saturation of potential solid phases with respect to time using elemental

Table 3
TEM X-ray EDS elemental composition of the precipitation products after respective times of both mineral wools (values were averaged at least 5 times in different areas of the sample).

Fig. 9	Sample	Elements (at. %)							
		O	Si	Ca	Al	Fe	Mg	Ti	Na
a	$^{1000}_{1d}S_{1M}$	45.4 ± 2.7	1.2 ± 0.2	1.9 ± 0.2	1.9 ± 0.4	7.8 ± 1.3	27.6 ± 1.4	1.6 ± 0.3	2.6 ± 0.4
b	$^{1000}_{1d}S_{1mM}$	51.3 ± 0.9	9.9 ± 0.5	3.3 ± 0.6	3.1 ± 0.2	6.4 ± 0.6	13.8 ± 0.4	1.2 ± 0.0	0.3 ± 0.1
c	$^{1000}_{7d}S_{1mM}$	59.9 ± 3.5	10.8 ± 2.0	2.3 ± 0.7	3.6 ± 0.5	2.2 ± 0.3	11.2 ± 1	0.4 ± 0.1	0.3 ± 0.0
d	$^{1000}_{30d}S_{1M}$	50.0 ± 4.2	13.6 ± 1.8	14.2 ± 2.1	0.3 ± 0.1	0.2 ± 0.0	0.1 ± 0.0	0.1 ± 0.0	6.8 ± 0.4
e	$^{50}_{30d}S_{1M}$	52.0 ± 3.9	17.2 ± 1.9	14.7 ± 2.1	1.6 ± 0.2	0.4 ± 0.1	0.05 ± 0.0	0.3 ± 0.0	5.2 ± 0.3
f	$^{1000}_{30d}G_{1M}$	55.7 ± 0.2	14.7 ± 0.1	11.7 ± 0.1	0.1 ± 0.0	0.1 ± 0.0	0.9 ± 0.0	0	4.4 ± 0.1
g	$^{50}_{30d}G_{1M}$	49.6 ± 0.1	18.9 ± 0.1	11.9 ± 0.1	0.5 ± 0.0	0.2 ± 0.0	3.4 ± 0.0	0	6.6 ± 0.1

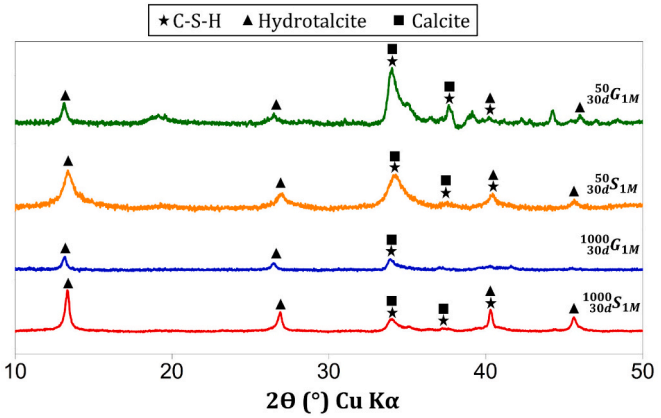

Fig. 10. XRD patterns in both Sw and Gw at both L/S ratios (1000 and 50) after 30 d in 1 M NaOH.

concentration which supports the experimentally formed phases during dissolution or alkali activation. Fig. 11 shows the saturation index of possible phases calculated according to the theoretical elemental concentrations [Section 3.2, Eq. (4)] with respect to time. The solid phases shown were selected based on the phases detected with dissolution of aluminosilicate glasses with similar compositions (basaltic glass for Sw, soda-lime glass for Gw) and experimental conditions used here [14,21,44–46]. There is no titanium phase reported in the CEM database, but titanium tends to precipitate as insoluble hydroxides at alkaline pH conditions [47]. Detailed chemical formulas of selected solid phases for this study are listed in Supporting Information, Table S3. As the calcium-aluminate-iron-silicate chemistry is diverse and multiple possible phases—for example, in case of calcium silicate hydrates (C-S-H) — the list is further shortlisted to saturation index of C-N-A-S-H phases (5CNA, INFCN, INFCNA) using CNASH_ss model as its formation is experimentally confirmed by SEM/TEM-EDS results. In case of stable Fe-siliceous hydrogarnets, $C_3FS_{0.84}H_{4.32}$ and $C_3FS_{1.34}H_{3.32}$ phases are used in this article as their formation in cement systems are kinetically supported to occur at ambient temperature conditions [41].

The results revealed that for both mineral wools and L/S conditions, the saturation of the iron hydroxides (FeOOHmic or geothite) was expected at all times and at both molarities, whereas brucite $Mg(OH)_2$ saturated at all times only with 1 M NaOH. This explains why Fe was under the detection limit throughout the dissolution studies at 1 mM & 1 M NaOH for both mineral wools and Mg at 1 M NaOH (Section 4.1). For mineral wools at both molarities, thermodynamic precipitation of brucite and Mg-Al-layered double hydroxide (LDH) occurs simultaneous with respect to each other; this is kinetically observed for sample $^{1000}S_{1mM}$, in which $Mg(OH)_2$ appeared to saturate from 10 h onwards (see Supporting Information, Fig. S1b), which correlates with the ICP results (Fig. 2a), where NL_{Mg} and NL_{Al} started to decrease exactly from 10 h and hydrotalcite-like structure precipitation was observed from the SEM images (Fig. 5c) and also in case of sample conditions $^{1000}S_{1M}$ (Fig. 6a) and $^{1000}G_{1M}$ (Fig. 7a). In case of $^{1000}G_{1mM}$, $Mg(OH)_2$ started to saturate from 3 d onwards, which correlates with the ICP results (Fig. 2b), where NL_{Mg} and NL_{Al} started to decrease exactly from 3 d and a precipitate layer was observed at 7d from the SEM images (Fig. 5d). However, NL_{Mg} for Gw continued to increase from 3 d to 7 d compared to NL_{Mg} of Sw in Fig. 2b. Al wt% is nearly 8.4 for Sw, whereas it is only 0.8 for Gw. As Al and Fe ions (and OH^-) majorly control the Mg availability in the solution by forming LDHs, the high content of dissolved Al and Fe will increase LDH precipitation for Sw, and consequently decrease Mg concentration in solution and NL_{Mg}. Magnesium silicate phases (M15SH, M075SH) was found to saturate at both molarities for both mineral wools but at different times. For $^{1000}_{1\ d-7d}S_{1mM}$, TEM-EDS (Fig. 9b-c) revealed the presence of phyllosilicate rich in Mg, but no

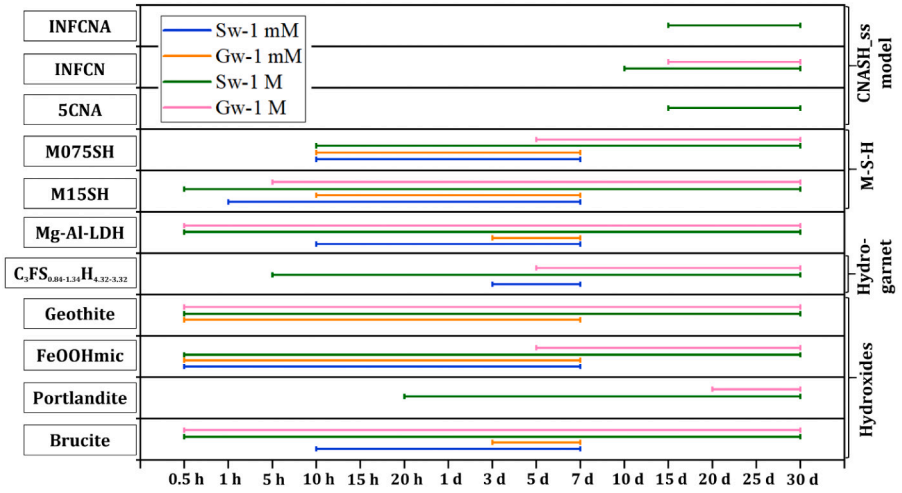

Fig. 11. Time intervals during which selected solid phases were supersaturated. Thermodynamic calculations were done according to the concentration of elements in samples with L/S 1000 based on the theoretical elemental release values according to Eq. (4) for (a) Sw in 1 mM NaOH (blue line) and (b) Gw (orange line) in 1 mM NaOH for time period 0.5 h to 7 d; (c) Sw (green line) in 1 M NaOH and (d) Gw (pink line) in 1 M NaOH for time period 0.5 h to 30 d, respectively. (For interpretation of the references to colour in this figure legend, the reader is referred to the web version of this article.)

separate magnesium silicate phase was observed and same in case of samples of $^{1000}S_{1M}$ and $^{1000}G_{1M}$. For $^{1000}G_{1mM}$, the Mg—Si phase saturation cannot be validated with any other results in this study. Siliceous hydrogarnet phases were thermodynamically predicted to saturate from 3d to 7 d for $^{1000}S_{1mM}$, 5 h to 30 d for $^{1000}S_{1M}$ and 5 d to 30 d for $^{1000}G_{1M}$. TEM-EDS and SEM images confirmed that no such phases were kinetically found to precipitate in samples of $^{1000}S_{1mM}$; instead, an Mg-rich phyllosilicate containing Na, Ca, Fe, Ti, and Si was observed to form from 1 to 7 d and for samples of $^{1000}G_{1M}$. However, for samples of $^{1000}S_{1M}$, nano (from 1 d) and globular domes (from 5 d) like structure of Ca, Si, Fe, Ti rich hydrogarnet like phases were kinetically confirmed to occur using TEM-EDS (Fig. 9d) and SEM images (Fig. 6 a-b).

Portlandite saturation was observed only with 1 M NaOH for both minerals, which shows that $Ca(OH)_2$ solubility decreases with an increase in pH, which is in line with ICP-OES results (Fig. 3-4). C-N-(A-)S-H "with" (5CNA, INFCNA) and "without" (INFCN) Al in their structure were observed to saturate with 1 M NaOH at both L/S ratios and for both mineral wools. TEM-EDS (Fig. 9d) and SEM analysis shows that formation of C-N-(A-)S-H with almost no Al (0.3 ± 0.1 % for Sw and 0.1 % for Gw)) in their structure was observed to form between after 10 d to 30 d for Sw and from 15 d for Gw which correlates with INFCN phase saturation from thermodynamic calculations. With L/S 50, the results show that $Ca(OH)_2$ and C-N-(A-)S-H saturation occurs earlier than with an L/S ratio of 1000 (see Supporting Information, Fig. S6). This is supported by the SEM results, as calcium silicate phase morphology formation occurs earlier at L/S 50 (from 2 d) than L/S 1000 (between 10 d–15d). TEM-EDS showed that C-N-(A-)S-H had increased Al (1.6 ± 0.2 % for Sw and 0.5 % for Gw) incorporated in its structure for both mineral wool at L/S 50 (Fig. 9e & g) which correlates with the thermodynamic calculation of INFCNA and 5CNA phase in Fig. S6. These calculations based on theoretical elemental concentrations [Eq. (4)] are slightly different in comparison to the calculations based on the experimentally detected concentrations (ICP-OES), especially at initial stages with L/S 1000, as there is a leaching of network modifiers, like Ca and Mg, and amphoteric cations, like Al, for both mineral wools at both molarities (See Figs. 2, 3a, 4a). Thus, some phases could be saturated earlier (like hydroxides and Mg-Al-LDH, See Tables S10-S13) than presented in Fig. 11 but no major effect of this early phase saturation was observed on the kinetics of real phases formation as they correlated well with the theoretical saturation of phases. A full list of saturation indexes calculated according to theoretical and experimentally detected values is provided in Supporting Information, Tables S4–S13.

5. Discussion

5.1. Dissolution and precipitation reactions

The initial dissolution rate (first 10 h) with high L/S ratio (1000) for both mineral wools at molarities 1 mM and 1 M were calculated (Table 4) based on the results in Figs. 2–4. Table 4 shows that there is a clear effect by the NaOH molarity and chemical composition on the dissolution rate. It is clearly evident that increasing the molarity of the NaOH solution from 1 mM to 1 M increases the normalized mass loss of Si, Al, and Ca and the total extent of dissolution of both mineral wools [14,25,27,31]. The initial dissolution rate implies that Sw and Gw dissolve roughly 4× and 2× faster in 1 M of NaOH, respectively, compared to dissolution in 1 mM of NaOH with L/S 1000. This is due to a higher hydroxyl ion concentration in 1 M of NaOH compared to 1 mM of NaOH, which accelerates the hydrolysis reaction by nucleophilic attack on network formers, such as Si and Al, on the mineral wool surface. At a low backward reaction progress condition like L/S 1000, the initial dissolution rate is mainly dependent on the chemical composition of the mineral wool and the reacting solution pH. Between the mineral wools at a constant molar concentration (1 mM or 1 M), Sw, which has more divalent ions and alumina, is more reactive according to initial dissolution rates than the high monovalent less alumina content Gw. This is due to the increased degree of depolymerization in Sw as opposed to Gw [48].

Table 4
Dissolution rates for both mineral wools at both molarities and L/S condition (1000) calculated using Eq. (3).

Experimental conditions	Rate of dissolution (μg/cm²/h)		
	Sw		Gw
	Initial rate	Residual rate	Initial rate
1 mM NaOH, L/S 1000	0.64	–	0.41
1 M NaOH, L/S 1000	2.50	0.10	0.73

At initial stages, leaching of ions is observed with a high L/S ratio (1000) and low pH conditions like 1 mM whereas with a low L/S ratio (50), it is decreased. These results are due to the higher proton concentration in 1 mM of NaOH compared to 1 M of NaOH and in high L/S ratio conditions (1000). Protons in the solution facilitate ion exchange and diffusion-controlled reactions like the leaching of Ca and Mg observed in Figs. 2, 3a, and 4a. Even though, leaching occurs at initial stages, congruent dissolution is supposed to be predominant at later stages of reaction at alkaline conditions [21] [13]. According to ab initio calculations, Al—O sites are preferred to undergo hydrolysis more easily than Si—O sites due to lower barrier energy for breaking the metal-oxygen (M-O) bond [49]. This may be the reason for the Al leaching observed in the initial stages of dissolution of the mineral wools with 1 M of NaOH. This kind of leaching of Ca, Mg, Al ions were also observed in other dissolution studies [50,51] and stone wool dissolution studies at pH 11–13 conditions [13].

The formation of precipitation products (including their elemental composition and formation kinetics) is dependent on the reacting solution chemistry (pH, L/S ratio, concentration of ions in the solution) and the chemical composition of the mineral wool. For both mineral wools, two types of main precipitates were observed: (a) Mg-Fe-Al-rich LDH precipitate, and (b) C-N-(A-)S-H precipitates. The driving force behind the precipitation reactions [26] was the saturation of the specific phases of metal ions with respect to the given solution conditions. At the early stages of dissolution, the precipitation of insoluble hydroxides of Fe (FeOOH, goethite), Mg (brucite), Ca (portlandite), and Ti occurs depending on the pH of the solution. SEM images of the thin layer-like precipitates observed in samples $^{1000}_{0.5\ h}S_{1mM}$, $^{50}_{0.5\ h}S_{1M}$ (see Supporting Information, Fig. S1 a and c, respectively), $^{1000}_{7d}G_{1mM}$ (Fig. 5d), and $_{0.5\ h}{}^{50}G_{1M}$ (Fig. 7c) may be the insoluble hydroxides, as their precipitation was supported by the PHREEQC results (see Supporting Information, Tables S4, S6, S5, and S9, respectively) and the ICP results. However, from the SEM-EDS analysis, a distinct hydroxide layer was not observed. These insoluble hydroxides were consumed to form LDHs of Mg, Fe, Al, and Ti, which was the nano-porous, platelet-like precipitate observed at both pH. In this study, phyllosilicates (saponite – Mg-rich smectite minerals) were favored in the case of 1 mM until 7 d, but the formation of LDHs were favored in the case of 1 M. The formation of phyllosilicates was observed for the dissolution of different glasses at a pH range of 8.5 to 12.5 in different studies [26,28,33,52,53]. Saponites are formed by the conversion of LDHs, where Al is substituted with Si oligomers at alkaline conditions [54]. This shows that this type of precipitation is kinetically and thermodynamically supported in the case of 1 mM but not in case of 1 M. For $^{1000}_{1d}S_{1M}$, before the formation of the LDHs, nano and globular micro domes of Fe siliceous hydrogarnet like structures rich in Ca, Si, Fe, and Ti were observed; and for $^{50}_{1d}S_{1M}$, meso-circular pillar-like structures were observed, as this can be another precipitation product. Evidence of the precipitation of Fe-siliceous rich hydrogarnets due to saturation is shown in PHREEQC (see Supporting Information, Table S6). No such dome structures were observed for $^{1000}G_{1M}$ and $^{50}G_{1M}$ at the nano and micro level even though their precipitation was thermodynamically supported.

At initial stages (until 24 h), comparing different L/S ratios at 1 M

NaOH, it was observed that the normalized mass loss of Sw and Gw at L/S 1000 was averagely 6× and 2× (including precipitation reactions) higher than at L/S 50, respectively. This could be because with L/S 1000, the feedback of dissolved species back to the mineral wool surface was low compared to L/S 50 conditions. This slow backward reaction progress (i.e., precipitation reaction) of L/S 1000 allowed the mineral wool to dissolve and maintain the forward rate; in contrast, in L/S 50, a fast backward reaction progress occurred, forming an amorphous gel by recondensation of dissolved species [39]. However, the effect is much more pronounced in Sw than Gw which can be due to the difference in chemical composition and the resulting surface precipitates.

Constant $NL_{Si,Al}$ values for samples of $^{1000}S_{1M}$ (15–30 d) and $^{50}S_{1M}$ (10–30 d) represents the residual rate regime which was observed only in the case of Sw, whereas a linear NL_{Si} values was observed for Gw samples of $^{1000}G_{1M}$ and $^{1000}G_{1M}$ system. This regime in Sw was reached faster with a decreasing L/S ratio due to increased saturation of the phase with respect to the solution. The rate fell to nearly zero at both L/S ratio conditions, but a minor residual rate (0.1 and 0.04 μg/cm^2/h for $^{1000}S_{1M}$ & $^{50}S_{1M}$, respectively) was still observed, showing that dissolution occurs, albeit slowly. From the literature, two explanations for the cause of the eventual rate drop and residual regime were mentioned: (1) the formation of an "amorphous porous hydrated gel" that acts as a protective diffusion barrier of ions, and (2) chemical affinity due to the saturation of dissolved species [34,39]. In our study, considering different L/S ratios, Sw had an eventual drop in NL_i values and residual rate regime, whereas Gw had a linear dissolution rate (representing linear NL_{Si} values) throughout the duration of the experiment. In Sections 4.2 and 4.3 (Tables 2 and 3), the amorphous gel, which was observed in both mineral wools and in both L/S ratios at later stages (30 d), was a C-N-(A-)S-H hydrate with low content of Al.

From Table 3, the Ca/Si ratios in the C-N-(A-)S-H precipitates of $^{1000}S_{1M}$, $^{50}S_{1M}$, $^{1000}G_{1M}$, and $^{50}G_{1M}$ were 1.04, 0.85, 0.79, and 0.63, respectively. The Na/Si ratios of $^{1000}S_{1M}$, $^{50}S_{1M}$, $^{1000}G_{1M}$, and $^{50}G_{1M}$ were 0.5, 0.3, 0.3, and 0.35, respectively. The Al/Si ratios of $^{1000}S_{1M}$, $^{50}S_{1M}$, $^{1000}G_{1M}$, and $^{50}G_{1M}$ were 0.02, 0.09, 0.007, and 0.03, respectively. In [14], it was reported that there was no rate drop due to the low Ca/Si molar ratio (0.54 to 0.78) of the highly porous C-S-H phase formed on the soda-lime silicate glass on dissolution with 1 M of NaOH. In theory, from comparing the Ca/Si values, the C-N-(A-)S-H precipitate of $^{1000}S_{1M}$ should act as a protective barrier more than that of $^{50}S_{1M}$ and reach an early residual regime state, but in reality the converse occurs. This shows that the eventual rate drop and residual regime is not entirely due to the kinetics of C-S-H formation. From the ICP solution analysis, for $^{1000}S_{1M}$, the molar Al/Si ratio showed that the residual regime from 15 to 30 d had a constant value of 0.8; and for $^{50}S_{1M}$ (from 10 to 30 d), the residual regime had a value of 0.85 (see Supporting Information, Fig. S7). Two major types of precipitate – Mg-Fe-Al LDH and C-N-(A-)S-H – were found on Sw at both L/S ratios. Calculating the average Al/Si molar ratio from these precipitates for samples $^{1000}_{15\ d}S_{1M}$ and $^{1000}_{30\ d}S_{1M}$ (from Table 2) gives an average value of 0.8. This shows that there is a possible equilibrium between the surface precipitates and the elemental composition of the solution [34]. Due to this approaching equilibrium, chemical affinity for further dissolution is slowed down, which causes the eventual rate drop and residual regime. From the perspective of the protective barrier of gel, from the Al/Si ratios of C-N-(A-)S-H precipitates, it was observed that decreasing the L/S ratio enhances Al incorporation in the C-N-(A-)S-H gel. Comparing the Al/Si ratio and the SEM/TEM-EDS of the C-N-(A-)S-H gel, it was visibly concluded that $^{50}S_{1M}$ had a low porosity structure due to the high Al/Si ratio in its structure. Most of the Al is preferred to be incorporated with Mg phases rather than in C-N-(A-)S-H phases in the high L/S ratio (see Section 4.5) but decreasing the L/S ratio facilitates the saturation of C-N-(A-)S-H phases with Al in their structure (like INFCNA and 5CNA). This is thermodynamically supported by the PHREEQC calculation, as seen in Supporting Information, Table S7. The high porous structure of $^{50}S_{1M}$ compared to the low porous structure of $^{1000}S_{1M}$ may cause a barrier in the transport of ions to the mineral wool surface, which slows down the dissolution. Additionally, from the SEM images of $^{1000}_{10d}S_{1M}$ in Fig. 6c, the Ca-rich layer that covered the entire surface of the mineral wool fiber and *meso* circular pillar like precipitate in Fig. 6e for $^{50}_{1\ d}S_{1M}$ can limit the transportation of ions. In the case of Gw, while the initial NL_{Si} was affected by the L/S ratio, the NL_{Si} at later stages were almost similar for both L/S ratios. This may be due to the following reasons: (i) surface precipitates are loosely attached to the mineral wool surface, always exposing the fiber surface to the solution and the highly porous surface precipitates (Fig. 7b and d), or (ii) equilibrium between the mineral wool surface/ precipitate to the solution is not yet reached, as in the case of Sw. Hence, eventual the rate drop and residual rate regime can be due to amorphous gel properties, chemical affinity due to approaching equilibrium between the mineral wool surface/ precipitates and the solution, or a combination of both depending upon the material composition and reacting solution properties.

Finally, the present study's results were compared with the dissolution rates of Sw and Gw at different experimental conditions from the literature (Table 5). It was observed that the dissolution rate for Sw was clearly higher at alkaline conditions compared to acidic or neutral pH. In contrast, for Gw, the dissolution rate at alkaline conditions was similar at pH 7.5, but higher compared to acidic conditions. However, as mentioned earlier, the experimental procedure (flow test in theliterature study, which greatly minimizes precipitation, whereas in this study precipitation occurs) and reacting solution composition (e.g., Gamble's solution has complex forming ions) [10] had a major impact on the calculated dissolution rates, and thus the results are not directly comparable, but rather give an approximate estimation.

6. Conclusions

Understanding the dissolution kinetics of mineral wool in alkaline conditions will be helpful in carefully customizing the mix design of the material for different applications. In this study, dissolution experiments of two types of mineral wools—stone wool and glass wool—at alkaline conditions at room temperature were carried out at two different L/S ratios. ICP-OES, SEM/STEM-EDS, and XRD analyses, as well as thermodynamic modelling, were employed to understand the dissolution kinetics and formation of precipitation products. The following conclusions were made based on the outcome of this experiment:

- The dissolution rate is affected by the reacting solution chemistry and material properties (both physical and chemical properties). The combination of initial leaching followed by congruent dissolution was presumed to be observed at a high L/S ratio and decreasing the L/S ratio decreases the leaching duration of the mineral wools at alkaline pH.
- At 1 M NaOH dissolution, Sw dissolves faster than Gw at a high L/S ratio (1000) in the later stages of dissolution; but at a low L/S ratio (50), Gw reacts almost the same as Sw. This is due to the formation of

Table 5
Comparison of dissolution rates measured in acidic and physiological pH with the alkaline pH of the present study.

Reference						Present study
Material	Experimental condition					Rate (in 1 M of NaOH, L/S1000) (values modified according to Ref. [10] conditions) (μg/cm^2/h)
	pH	L/S	Days	Reagent	Rate (μg/cm^2/h)	
Stone wool [10]	4.5 7.5	1666	28	HCl Gamble soln.	0.022 0.010	0.346 (for 15 days)
Glass wool [10]	4.5 7.5	1666	28	HCl Gamble soln.	0.002 0.163	0.169 (for 30 days)

a residual regime (or induction period) observed in Sw as a result of the combination of equilibrium between the surface precipitates & the solution chemistry and the protective barrier properties of precipitates for the transport of ions. The residual regime was not observed in the case of Gw can be due to i) the surface precipitates were loosely attached and exposed the fiber surface to the solution ii) chemical affinity between the surface precipitates and solution chemistry is not reached yet.

- A dissolution-precipitation mechanism occurs for mineral wools at alkaline conditions. Two types of precipitation product were observed: (1) Mg-Al-Fe LDH-type phase in the case of 1 M, and phyllosilicates in the case of 1 mM only for Sw; (2) C-N-(A-)S-H phase with a small amount of Al only observed at 1 M conditions. Mg—Fe rich precipitate forms around the dissolving mineral wool surface, whereas C-N-(A-)S-H grows in contact with the solution (Fig. 8a).
- Al was observed to incorporate in LDH rather than to C-N-S-H at high L/S conditions (1000), leading to a highly porous, weak C-N-S-H structure; whereas at low L/S conditions (50), Al starts to incorporate into a C-N-S-H gel to form C-N-(A-)S-H, resulting in a small, highly porous, strong C-N-(A-)S-H structure.
- New findings of precipitates due to the presence of Ti in the stone wool composition were observed during the dissolution of Sw in 1 M of NaOH at L/S 1000: Ti in the LDH structure and hydrogarnets like Ca-Fe-Ti (nano-domes at 1 d) & Ca-Si-Ti precipitates (globular micro-domes at 5 d).
- The insights gained in this study are important for the development of alkali-activated basalt glass and soda-lime silicate glass binders and, additionally, their incorporation in cement systems as the conditions are similar to cement pore solutions.

CRediT authorship contribution statement

Rajeswari Ramaswamy: Conceptualization, Methodology, Investigation, Formal analysis, Software, Visualization, Validation, Writing – original draft, Writing – review & editing. **Juho Yliniemi:** Conceptualization, Methodology, Visualization, Validation, Writing – review & editing, Project administration, Supervision, Funding acquisition. **Mirja Illikainen:** Supervision, Funding acquisition.

Declaration of competing interest

The authors declare that they have no known competing financial interests or personal relationships that could have appeared to influence the work reported in this paper.

Data availability

Data will be made available on request.

Acknowledgements

This work was funded by the European Union's Horizon 2020 project, called “Wool2loop,” under grant agreement No. 821000. Juho Yliniemi was funded by the Academy of Finland (grant # 322786). Techniques for the characterization of materials were conducted with the support of the Centre of Material Analysis, University of Oulu, Finland. Lab technicians at the Fibre and Particle Engineering Unit, Mr. Jarno Karvonen, Mr. Jani Österlund, and Elisa Wirkkala, carried out laboratory analysis and guided some of the experimental procedures. The authors would like to acknowledge the support received from the project funding and the fruitful discussions between the co-authors throughout the article writing process, and they are grateful for the help received from the lab technicians at the Centre of Material Analysis and at the Fibre and Particle Engineering Unit during the challenging period of the COVID-19 pandemic.

Appendix A. Supplementary data

Supplementary data to this article can be found online at https://doi.org/10.1016/j.cemconres.2022.106922.

References

[1] O. Väntsi, T. Kärki, Mineral wool waste in Europe: a review of mineral wool waste quantity, quality, and current recycling methods, J. Mater. Cycles Waste Manag. 16 (2014) 62–72, https://doi.org/10.1007/s10163-013-0170-5.
[2] J. Yliniemi, B. Walkley, J.L. Provis, P. Kinnunen, M. Illikainen, Nanostructural evolution of alkali-activated mineral wools, Cem. Concr. Compos. 106 (2020), 103472, https://doi.org/10.1016/j.cemconcomp.2019.103472.
[3] P. Kinnunen, J. Yliniemi, B. Talling, M. Illikainen, Rockwool waste in fly ash geopolymer composites, J. Mater. Cycles Waste Manag. 19 (2017) 1220–1227, https://doi.org/10.1007/s10163-016-0514-z.
[4] R. Kubiliute, R. Kaminskas, A. Kazlauskaite, Mineral wool production waste as an additive for Portland cement, Cem. Concr. Compos. 88 (2018) 130–138, https://doi.org/10.1016/j.cemconcomp.2018.02.003.
[5] A. Cheng, W.T. Lin, R. Huang, Application of rock wool waste in cement-based composites, Mater. Des. 32 (2011) 636–642, https://doi.org/10.1016/j.matdes.2010.08.014.
[6] S.A. Bernal, J.L. Provis, A. Fernández-jiménez, P.V. Krivenko, E. Kavalerova, M. Palacios, C. Shi, Alkali Activated Materials, 2014, https://doi.org/10.1007/978-94-007-7672-2.
[7] A. Hajimohammadi, J.S.J. van Deventer, Dissolution behaviour of source materials for synthesis of geopolymer binders: a kinetic approach, Int. J. Miner. Process. 153 (2016) 80–86, https://doi.org/10.1016/j.minpro.2016.05.014.
[8] A. Hajimohammadi, J.L. Provis, J.S.J. Van Deventer, Effect of alumina release rate on the mechanism of geopolymer gel formation, Chem. Mater. 22 (2010) 5199–5208, https://doi.org/10.1021/cm101151n.
[9] H. Xu, J.S.J. Van Deventer, The geopolymerisation of alumino-silicate minerals, Int. J. Miner. Process. 59 (2000) 247–266, https://doi.org/10.1016/S0301-7516(99)00074-5.
[10] A. Cannizzaro, S. Canepari, M.L. Astolfi, S. Iavicoli, F. Angelosanto, A. Campopiano, A. Olori, D. Ramires, Dissolution of glass wool, rock wool and alkaline earth silicate wool: morphological and chemical changes in fibers, Regul. Toxicol. Pharmacol. 70 (2014) 393–406, https://doi.org/10.1016/j.yrtph.2014.05.023.
[11] V.R. Christensen, S. Lund Jensen, M. Guldberg, O. Kamstrup, Effect of chemical composition of man-made vitreous fibers on the rate of dissolution in vitro at different pHs, Environ. Health Perspect. 102 (1994) 83–86, https://doi.org/10.2307/3432064.
[12] M. Guldberg, V.R. Christensen, M. Perander, B. Zoitos, A.R. Koenig, K. Sebastian, Measurement of in-vitro fibre dissolution rate at acidic pH, Ann. Occup. Hyg. 42 (1998) 233–243, https://doi.org/10.1016/S0003-4878(98)00026-X.
[13] D.V. Okhrimenko, S.H.Q. Barly, M. Jensen, L.Z. Lakshtanov, D.B. Johansson, M. Solvang, Y.Z. Yue, S.L.S. Stipp, Surface evolution of aluminosilicate glass fibers during dissolution: influence of pH, solid-to-solution ratio and organic treatment, J. Colloid Interface Sci. 606 (2022) 1983–1997, https://doi.org/10.1016/j.jcis.2021.09.148.
[14] H. Maraghechi, F. Rajabipour, C.G. Pantano, W.D. Burgos, Effect of calcium on dissolution and precipitation reactions of amorphous silica at high alkalinity, Cem. Concr. Res. 87 (2016) 1–13, https://doi.org/10.1016/j.cemconres.2016.05.004.
[15] P. Duxson, J.L. Provis, Designing precursors for geopolymer cements, J. Am. Ceram. Soc. 91 (2008) 3864–3869, https://doi.org/10.1111/j.1551-2916.2008.02787.x.
[16] Iarc, in: IARC Working Group on the Evaluation of Carcinogenic Risks to Humans, International Agency for Research on Cancer Iarc Monographs on the Evaluation of Carcinogenic Risks To Humans, Iarc Monogr. Eval. Carcinog. Risks To Humans 80, 2002, p. 338, https://doi.org/10.1002/food.19940380335, 27.
[17] J. Yliniemi, R. Ramaswamy, T. Luukkonen, O. Laitinen, in: Characterization of Mineral Wool Waste Chemical Composition, Organic Resin Content and Fiber Dimensions: Aspects for Valorization 131, 2021, pp. 323–330, https://doi.org/10.1016/j.wasman.2021.06.022.
[18] R.C. Brown, P.T.C. Harrison, Alkaline earth silicate wools - a new generation of high temperature insulation, Regul. Toxicol. Pharmacol. 64 (2012) 296–304, https://doi.org/10.1016/j.yrtph.2012.08.020.
[19] M.A. Moore, R.C. Brown, G. Pigott, in: MATERIAL PROPERTIES OF MMVFs, 2001, pp. 1117–1149.
[20] F.R. Jones, N.T. Huff, The Structure and Properties of Glass Fibres, Woodhead Publishing Limited, 2009, https://doi.org/10.1533/9781845697310.3.307.
[21] J.L. Crovisier, J. Honnorez, J.P. Eberhart, Dissolution of basaltic glass in seawater: mechanism and rate, Geochim. Cosmochim. Acta 51 (1987) 2977–2990, https://doi.org/10.1016/0016-7037(87)90371-1.
[22] E.M. Pierce, E.A. Rodriguez, L.J. Calligan, W.J. Shaw, B. Pete McGrail, An experimental study of the dissolution rates of simulated aluminoborosilicate waste glasses as a function of pH and temperature under dilute conditions, Appl. Geochemistry. 23 (2008) 2559–2573, https://doi.org/10.1016/j.apgeochem.2008.05.006.
[23] S. Gin, P. Frugier, P. Jollivet, F. Bruguier, E. Curti, New insight into the residual rate of borosilicate glasses: effect of s/v and glass composition, Int. J. Appl. Glas. Sci. 4 (2013) 371–382, https://doi.org/10.1111/ijag.12048.

[24] P.V. Brady, J.V. Walther, Controls on silicate dissolution rates in neutral and basic pH solutions at 25°C, Geochim. Cosmochim. Acta 53 (1989) 2823–2830, https://doi.org/10.1016/0016-7037(89)90160-9.
[25] S. Gin, P. Jollivet, M. Fournier, C. Berthon, Z. Wang, A. Mitroshkov, Z. Zhu, J. V. Ryan, The fate of silicon during glass corrosion under alkaline conditions: a mechanistic and kinetic study with the international simple glass, Geochim. Cosmochim. Acta 151 (2015) 68–85, https://doi.org/10.1016/j.gca.2014.12.009.
[26] C.A. Utton, R.J. Hand, N.C. Hyatt, S.W. Swanton, S.J. Williams, Formation of alteration products during dissolution of vitrified ILW in a high-pH calcium-rich solution, J. Nucl. Mater. 442 (2013) 33–45, https://doi.org/10.1016/j.jnucmat.2013.08.026.
[27] S. Mercado-Depierre, F. Angeli, F. Frizon, S. Gin, Antagonist effects of calcium on borosilicate glass alteration, J. Nucl. Mater. 441 (2013) 402–410, https://doi.org/10.1016/j.jnucmat.2013.06.023.
[28] B.M.J. Thien, N. Godon, A. Ballestero, S. Gin, A. Ayral, The dual effect of mg on the long-term alteration rate of AVM nuclear waste glasses, J. Nucl. Mater. 427 (2012) 297–310, https://doi.org/10.1016/j.jnucmat.2012.05.025.
[29] H. Aréna, N. Godon, D. Rébiscoul, P. Frugier, R. Podor, E. Garcès, M. Cabie, J. P. Mestre, Impact of iron and magnesium on glass alteration: characterization of the secondary phases and determination of their solubility constants, Appl. Geochem. 82 (2017) 119–133, https://doi.org/10.1016/j.apgeochem.2017.04.010.
[30] R. Snellings, Solution-controlled dissolution of supplementary cementitious material glasses at pH 13: the effect of solution composition on glass dissolution rates, J. Am. Ceram. Soc. 96 (2013) 2467–2475, https://doi.org/10.1111/jace.12480.
[31] C.A. Utton, R.J. Hand, P.A. Bingham, N.C. Hyatt, S.W. Swanton, S.J. Williams, Dissolution of vitrified wastes in a high-pH calcium-rich solution, J. Nucl. Mater. 435 (2013) 112–122, https://doi.org/10.1016/j.jnucmat.2012.12.032.
[32] S. Mercado-Depierre, M. Fournier, S. Gin, F. Angeli, Influence of zeolite precipitation on borosilicate glass alteration under hyperalkaline conditions, J. Nucl. Mater. 491 (2017) 67–82, https://doi.org/10.1016/j.jnucmat.2017.04.043.
[33] S. Gin, J.P. Mestre, SON, 68 nuclear glass alteration kinetics between pH 7 and pH 11.5, J. Nucl. Mater. 295 (2001) 83–96, https://doi.org/10.1016/S0022-3115(01)00434-2.
[34] T. Antonić, C. Kosanović, B. Subotić, A. Čižmek, Dissolution of amorphous aluminosilicate zeolite precursors in alkaline solutions. Part 1. - Kinetics of the dissolution, J. Chem. Soc. Faraday Trans. 89 (1993) 1817–1822, https://doi.org/10.1039/FT9938901817.
[35] E. Vernaz, S. Gin, C. Jégou, I. Ribet, Present understanding of r7t7 glass alteration kinetics and their impact on long-term behavior modeling, J. Nucl. Mater. 298 (2001) 27–36, https://doi.org/10.1016/S0022-3115(01)00643-2.
[36] C.L. Corkhill, N.J. Cassingham, P.G. Heath, N.C. Hyatt, Dissolution of UK high-level waste glass under simulated hyperalkaline conditions of a colocated geological disposal facility, Int. J. Appl. Glas. Sci. 4 (2013) 341–356, https://doi.org/10.1111/ijag.12042.
[37] T. Chave, P. Frugier, S. Gin, A. Ayral, Glass-water interphase reactivity with calcium rich solutions, Geochim. Cosmochim. Acta 75 (2011) 4125–4139, https://doi.org/10.1016/j.gca.2011.05.005.
[38] S. Ribet, S. Gin, Role of neoformed phases on the mechanisms controlling the resumption of SON68 glass alteration in alkaline media, J. Nucl. Mater. 324 (2004) 152–164, https://doi.org/10.1016/j.jnucmat.2003.09.010.
[39] P. Frugier, S. Gin, Y. Minet, T. Chave, B. Bonin, N. Godon, J.E. Lartigue, P. Jollivet, A. Ayral, L. De Windt, G. Santarini, SON68 nuclear glass dissolution kinetics: current state of knowledge and basis of the new GRAAL model, J. Nucl. Mater. 380 (2008) 8–21, https://doi.org/10.1016/j.jnucmat.2008.06.044.
[40] M. Fournier, S. Gin, P. Frugier, Resumption of nuclear glass alteration: state of the art, J. Nucl. Mater. 448 (2014) 348–363, https://doi.org/10.1016/j.jnucmat.2014.02.022.
[41] B. Lothenbach, D.A. Kulik, T. Matschei, M. Balonis, L. Baquerizo, B. Dilnesa, G. D. Miron, R.J. Myers, Cemdata18: a chemical thermodynamic database for hydrated Portland cements and alkali-activated materials, Cem. Concr. Res. 115 (2019) 472–506, https://doi.org/10.1016/j.cemconres.2018.04.018.
[42] A.R. West, Solid State Chemistry and Its Applications, 2014, https://doi.org/10.1107/s0108768185002476.
[43] N. Valle, A. Verney-Carron, J. Sterpenich, G. Libourel, E. Deloule, P. Jollivet, Elemental and isotopic (29Si and 18O) tracing of glass alteration mechanisms, Geochim. Cosmochim. Acta 74 (2010) 3412–3431, https://doi.org/10.1016/j.gca.2010.03.028.
[44] A. Abdelouas, J.L. Crovisier, W. Lutze, B. Fritz, A. Mosser, R. Müller, Formation of hydrotalcite-like compounds during R7T7 nuclear waste glass and basaltic glass alteration, Clay Clay Miner. 42 (1994) 526–533, https://doi.org/10.1346/CCMN.1994.0420503.
[45] S.R. Gislason, E.H. Oelkers, Mechanism, rates, and consequences of basaltic glass dissolution: II. An experimental study of the dissolution rates of basaltic glass as a function of pH and temperature, Geochim. Cosmochim. Acta 67 (2003) 3817–3832, https://doi.org/10.1016/S0016-7037(00)00176-5.
[46] V. Daux, G. Christophe, T. Advocat, J.L. Crovisier, P. Stille, Kinetic aspects of basaltic glass dissolution at 90°C: role of aqueous silicon and aluminium, Chem. Geol. 142 (1997) 109–126, https://doi.org/10.1016/S0009-2541(97)00079-X.
[47] T. Kokubo, H. Takagi, M. Tashiro, Alkaline durability of BaOTiO2SiO2 glasses, J. Non-Cryst. Solids 52 (1982) 427–433, https://doi.org/10.1016/0022-3093(82)90317-9.
[48] A. Schöler, F. Winnefeld, M. Ben Haha, B. Lothenbach, The effect of glass composition on the reactivity of synthetic glasses, J. Am. Ceram. Soc. 100 (2017) 2553–2567, https://doi.org/10.1111/jace.14759.
[49] C.P. Morrow, S. Nangia, B.J. Garrison, Ab initio investigation of dissolution mechanisms in aluminosilicate minerals, J. Phys. Chem. A 113 (2009) 1343–1352, https://doi.org/10.1021/jp8079099.
[50] T. Oey, E.C. La Plante, G. Falzone, K. Yang, A. Wada, M. Bauchy, J.W. Bullard, G. Sant, Topological controls on aluminosilicate glass dissolution: complexities induced in hyperalkaline aqueous environments, J. Am. Ceram. Soc. 103 (2020) 6198–6207, https://doi.org/10.1111/jace.17357.
[51] I. Nikolić, A. Drinčić, D. Djurović, L. Karanović, V.V. Radmilović, V.R. Radmilović, Kinetics of electric arc furnace slag leaching in alkaline solutions, Constr. Build. Mater. 108 (2016) 1–9, https://doi.org/10.1016/j.conbuildmat.2016.01.038.
[52] W. Lutze, G. Malow, R.C. Ewing, M.J. Jercinovic, K. Keil, Alteration of basalt glasses: implications for modelling the long-term stability of nuclear waste glasses, Nature 314 (1985) 252–255, https://doi.org/10.1038/314252a0.
[53] E. Curti, in: Long-term Corrosion of Two Nuclear Waste Reference Glasses (MW and SON68): A Kinetic and Mineral Alteration Study 21, 2006, pp. 1152–1168, https://doi.org/10.1016/j.apgeochem.2006.03.010.
[54] Q. Tao, Q. Zeng, M. Chen, H. He, S. Komarneni, Formation of saponite by hydrothermal alteration of metal oxides: implication for the rarity of hydrotalcite, Am. Mineral. 104 (2019) 1156–1164, https://doi.org/10.2138/am-2019-7043.